

# **LEGIBILITY NOTICE**

**A major purpose of the Technical Information Center is to provide the broadest dissemination possible of information contained in DOE's Research and Development Reports to business, industry, the academic community, and federal, state and local governments.**

**Although portions of this report are not reproducible, it is being made available in microfiche to facilitate the availability of those parts of the document which are legible.**

**LA-UR** -87-1268  
Final

LA-UR--87-1268

DE88 000521

CONF-870622--1C

Los Alamos National Laboratory is operated by the University of California for the United States Department of Energy under contract W-7405-ENG-36

**TITLE:** COMPARISON OF SIDEBAND SPECTRA OBTAINED FROM ANALYTICAL FORMULA  
AND FROM NUMERICAL SIMULATION IN FREE-ELECTRON LASER

**AUTHOR(S):** H. Takeda

**SUBMITTED TO:** AIAA 19th Fluid Dynamics, Plasma Dynamics and Lasers Conference  
Honolulu, Hawaii, June 8-10, 1987

#### DISCLAIMER

This report was prepared as an account of work sponsored by an agency of the United States Government. Neither the United States Government nor any agency thereof, nor any of their employees, makes any warranty, express or implied, or assumes any legal liability or responsibility for the accuracy, completeness, or usefulness of any information, apparatus, product, or process disclosed, or represents that its use would not infringe privately owned rights. Reference herein to any specific commercial product, process, or service by trade name, trademark, manufacturer, or otherwise does not necessarily constitute or imply its endorsement, recommendation, or favoring by the United States Government or any agency thereof. The views and opinions of authors expressed herein do not necessarily state or reflect those of the United States Government or any agency thereof.

By acceptance of this article, the publisher recognizes that the U S Government retains a nonexclusive, royalty-free license to publish or reproduce the published form of this contribution, or to allow others to do so, for U S Government purposes

The Los Alamos National Laboratory requests that the publisher identify this article as work performed under the auspices of the U S Department of Energy

**MASTER**

**Los Alamos** Los Alamos National Laboratory  
Los Alamos, New Mexico 87545

*mg*

# COMPARISON OF SIDEBAND SPECTRA OBTAINED FROM ANALYTICAL FORMULA AND FROM NUMERICAL SIMULATION IN FREE-ELECTRON LASER\*

Harunori Takeda

Los Alamos National Laboratory  
MS E531, Los Alamos, NM 87545

## Abstract

The sideband spectrum appearing in the free-electron laser is analyzed. For an untapered undulator, we predict the wavelengths of local peaks arising from the sidebands; they are compared with numerical simulations. In our analytical theory, three laser-driving terms are derived: One term does not chirp in frequency, drives a number of frequencies simultaneously, and is always the strongest term with a fixed strength. The other two driving terms, which also drive multiple frequencies, chirp to both directions from a resonant frequency. We assume that the sidebands originate from a dipole oscillation of average electron energy. This oscillation frequency is equal to the synchrotron oscillation frequency. The theory predicts that the strength of the chirping terms is proportional to the amplitude of the dipole moment.

## Introduction

Sidebands reduce the extraction efficiency and the gain of a free-electron laser (FEL) with a tapered undulator. On the other hand, the sidebands occurring in an untapered FEL undulator increase the extraction efficiency and the gain. In an oscillator experiment, the laser light is amplified between two mirrors. In this paper we discuss the spectral characteristics of sidebands occurring in the untapered undulator and the local peaks of the laser spectrum when new sidebands are excited and their intensities are increased as the pass number of the laser radiation in the cavity increases.

To explain the spectral characteristics of the sideband, we extend the multifrequency formulation of the free-electron laser<sup>1</sup> by including a simple oscillator that represents the sideband. The frequency of the oscillator is assumed equal to the synchrotron oscillation frequency of the electrons in the ponderomotive potential well. Using this theory, we derive a relation between the frequency separation of each sideband and the bandwidth of the fundamental. We also derive that the synchrotron motion induces frequency chirpings of the laser from the resonant frequency. Two sideband driving terms arise from a single resonant frequency that splits in opposite directions.

We relate the synchrotron period and the undulator length as a function of frequency chirp. The numerical simulation shows the same frequency chirp of the peak intensity as the analytically obtained frequency chirp.

To confirm the picture of sidebands obtained from the analytical study, we simulated an FEL oscillator experiment using a one-dimensional FEL code, FELP,\*\* assuming that no laser intensity is lost in the optical cavity. An untapered undulator is placed at the center of the cavity. The laser in the multipass numerical simulation starts with noise characterized by wide bandwidth, random phase, and random amplitude. The starting intensity is set such that it induces the synchrotron oscillation with a period greater than the undulator length. Laser spectra are calculated by taking snapshots at several pass numbers. Then, the local peaks of the spectra are compared to the predicted peaks from the analytical expression.

## Electrons Driven by a Multifrequency Laser

Using the one-dimensional approximation, we include both the fundamental and the sidebands in the electron equation of motion by expressing the optical field as superposed waves. Defining the vector potentials of the optical field and helical undulator as

$$\vec{A}_L = \sum_k A_{Lk}(z) [\vec{x} \cos(\theta_{Lk} - \omega_{Lk}t + \phi_{Lk}) - \vec{y} \sin(\theta_{Lk} - \omega_{Lk}t + \phi_{Lk})] \quad (1)$$

and

$$\vec{A}_u = -A_u(z) [\vec{x} \cos \theta_u + \vec{y} \sin \theta_u] \quad (2)$$

where

$$\theta_u = \int_0^z k_u dz \quad (3)$$

and

$$\theta_{Lk} = k_{Lk} z \quad (4)$$

\* Work performed under the auspices of the U.S. Dept. of Energy and supported by the U.S. Army Strategic Defense Command

\*\* FELP is a one-dimensional free-electron laser code written by H. D. McVey, MS-E531, Los Alamos National Laboratory, Los Alamos, NM 87545.

The phase angle of an electron for a wave number  $k$  can be defined as

$$\Psi_k = k_L z + \int_0^z k_u dz - \omega_{Lk} t + \phi_{Lk} . \quad (5)$$

Following the standard derivation using Hamilton's equation, one can obtain the energy equation

$$\frac{d\gamma}{dt} = -\frac{a_u(z)}{\gamma} \sum_k \omega_{Lk} a_{Lk}(z) \sin \Psi_k(z, t) , \quad (6)$$

where  $a_u$  and  $a_{Lk}$  are dimensionless vector potentials of the undulator and the laser, respectively, with wave number  $k$ . The laser frequency is defined as  $\omega_{Lk} = ck_L$ . The time derivative of the electron phase angle is

$$\frac{d\Psi_k}{dt} = c\beta_z \left( k_u - \frac{1 + \bar{\alpha}^2}{(1 + \beta_z)\beta_z\gamma^2} k_L \right) + \frac{d\phi_k}{dt} , \quad (7)$$

where  $\bar{\alpha}$  is defined as a sum of dimensionless vector potentials of the laser and the undulator  $(= \frac{e}{m_0 c \gamma} (A_u + A_L))$ .

In the presence of a frequency spread, the buckets from each wave number  $k$  are superposed, causing the electrons to be detrapped from the bucket of the resonant frequency.

### Model of Sideband

It is generally accepted that the sideband is driven by a periodic motion of electrons in the bucket. The sideband appears in the laser spectrum as an added frequency in addition to the fundamental frequency. To have gain at the sideband frequency, the laser must be driven by the transverse motion of electrons at that frequency. Therefore, the transverse motion of the electrons must possess sideband frequencies. The transverse velocity and the total electron energy are related by  $\beta_\perp = \frac{1}{\gamma} a$  (where  $a$  is the transverse dimensionless vector potential of the field); we note that the driving of the sideband is not directly related to the longitudinal position of the electrons in the bucket. When the electrons are localized and oscillate in the longitudinal phase space, the transverse motion resulting from the oscillation drives the laser field at the corresponding sideband frequencies.

When an electron beam with a small energy spread enters an undulator, the electrons see a number of buckets: each bucket corresponds to a bucket of a particular laser frequency and phase. However, the energy transfer from the electrons to the laser is maximum where the peak gain is equal to the electron-beam energy. Also, a laser field with shorter wavelength having a negative gain at the electron-beam energy (as created by spontaneous emission or noise) gives energy to the electron beam. Then the energy is transferred from a short wavelength to a long fundamental wavelength.

Because the energy at which peak gain occurs for the fundamental is higher than the beam energy, the average energy of the electrons is higher than the resonant energy of that bucket. The average energy of the electrons oscillates around the resonant particle of the bucket. This oscillation frequency is approximately the synchrotron frequency with respect to that bucket. As the amplitude of the fundamental increases and sidebands are generated at longer wavelengths, lower resonant energies of corresponding buckets from sidebands reduce the oscillation center of the average electron energy, and a further detrapping from the bucket of the fundamental occurs. This action causes a net positive gain and increased efficiency for an untapered undulator.

The energy of the  $j$ th electron as a function of time can be approximated as

$$\gamma_j = \gamma_0 + \gamma_1 \cos(\omega_s t + \phi_s) , \quad (8)$$

where  $\omega_s$  is the average energy oscillation frequency that is approximately the synchrotron frequency,  $\gamma_0$  is the average energy of the oscillation center, and  $\gamma_1$  is the average energy oscillation amplitude. The phase angle  $\phi_s$  of the average energy oscillation at the undulator entrance is left unknown; assuming  $\phi_s \sim 0$  appears reasonable, but it violates the observed tendency that the intensity-weighted wavelength of the spectrum chirps longer because of the sideband.

Let us assume that two sidebands are present at frequencies equally displaced about the resonant frequency. When electrons enter the undulator with uniform phase-angle distribution, the sum of the driving terms over the electrons is zero. However after a short distance in the undulator, the energy of the electrons is increased by absorption from the sidebands. Each sideband has the following wave number: one wave number with  $k_R + \delta k$  above the resonance  $k_R$  and the other with  $k_R - \delta k$ . Assuming that the shift of the laser field phase at wave number  $k_R$  is small, the electron phase angle  $\Psi_{k_R+\delta k}$  reduces. The other phase angle  $\Psi_{k_R-\delta k}$  increases by the same amount. For an untapered undulator, Eq. (6) gives a net positive energy to electrons from the sidebands. This result implies that the phase angle  $\phi_s$  is approximately  $\pi$  for the untapered undulator.

Restating the assumption of Eq. (8): Each electron energy is replaced by an average energy that oscillates around a sideband-modified resonant energy  $\gamma_0$ . Although the sideband-modified resonant energy is not well defined, it is determined from the emerging buckets resulting from the presence of sidebands. The phase distribution of the electrons contributes gain to both fundamental and sidebands, but it does not directly drive the sidebands.

Substituting Eq. (8) into  $\beta_{\perp} = \frac{|\mathbf{a}|}{\gamma}$ , and assuming that the ratio of bucket height to the resonant energy is small, one obtains the following transverse electron velocity modulated by the synchrotron oscillation:

$$\begin{aligned}\beta_z &= a_w \frac{\cos(k_w \beta_z c t + \phi_0)}{\gamma_0 \left[ 1 + \frac{2b}{\gamma_0} \cos(\omega_s t + \phi_s) \right]} \\ &\approx \frac{a_w}{\gamma_0} \left[ 1 - \frac{\gamma_b}{\gamma_0} \cos(\omega_s t + \phi_s) \right] \cos(k_w \beta_z c t + \phi_0) \\ &= \frac{a_w}{4\gamma_0} \left\{ 2e^{j(\omega t + \phi_0)} - \frac{\gamma_b}{\gamma_0} e^{j[(\omega - \omega_s)t - \phi_s + \phi_0]} - \frac{\gamma_b}{\gamma_0} e^{j[(\omega + \omega_s)t + \phi_s + \phi_0]} \right\} + C.C.,\end{aligned}\quad (9)$$

where the electron transverse frequency is  $\omega = ck_w \beta_z$ , and C.C. means complex conjugate. Equation (9) states that the electron transverse motion, in fact, has  $\pm\omega_s$  modulated frequency components. The radiation field is driven by the transverse electron current, and two sidebands are driven by the transverse motion. The strength of each component is measured by the relative energy  $\frac{\gamma_b}{\gamma_0}$ . A sideband component is weaker than the fundamental by a factor  $\frac{\gamma_b}{\gamma_0}$ , which is, at most, a gain bandwidth of the undulator.

#### Single Frequency Component of Spectral Equation for an Untapered Undulator

A single frequency component of the field is obtained by integrating both sides of the spectrally decomposed laser equation (derived in Ref. 1), with respect to  $\tau$  after multiplying by  $e^{i\omega_1 \tau}$  on both sides of the equation. The  $i$ th component in the left-hand side (LHS) of the spectrally decomposed laser equation is

$$\begin{aligned}&K \sum_{k,a} \frac{2g_{ka}}{\sqrt{\omega_k}} i k \hat{e}^a e^{i\phi_{ka}} \left( \int_0^{\tau_1} e^{i(\omega_1 - \omega_k)\tau} d\tau \right) \left( \frac{\partial f_{ka}}{\partial z_1} + i \frac{\partial \phi_{ka}}{\partial z_1} f_{ka} \right) \\ &= K \tau_1 \frac{2g_{ka}}{\sqrt{\omega_k}} i k \hat{e}^a e^{i\phi_{ka}} \left( \frac{\partial f_{ka}}{\partial z_1} + i \frac{\partial \phi_{ka}}{\partial z_1} f_{ka} \right).\end{aligned}\quad (10)$$

We include the sideband in the laser equation as follows: using the following relations that relate the variables  $\tau$  and  $z_1$  to the variables  $t$  and  $z$ ,

$$z = z_1 + \frac{\beta_z c}{1 - \beta_z} \tau$$

and

$$t = \frac{z_1}{c} + \frac{1}{1 - \beta_z} \tau,$$

we substitute the second equation above into Eq. (8), and using  $z_{1j} = \frac{z_1}{1 - \beta_{zj}}$ , the spectrally decomposed field equation can be approximated to first order in  $\frac{2b}{\gamma_0}$ . The  $i$ th laser wave-number component in the right-hand side (RHS) of the spectrally decomposed laser equation is then given by (see Ref. 1 for definition of terms)

$$\begin{aligned}&\sum_j \frac{\delta(z_1 - z_{1j})}{(1 - \beta_{zj})\gamma_0} \sum_{k,a} \frac{g_{ka}}{\sqrt{\omega_k}} \hat{e}^a \int_0^{\tau_1} e^{i(\omega_1 - \omega_{ka})\tau} d\tau e^{i\phi_{ka}} f_{ka} \\ &+ F \sum_j \frac{\delta(z_1 - z_{1j})}{(1 - \beta_{zj})\gamma_0} \int_0^{\tau_1} e^{i\left(\omega_1 - k_w \frac{z_1 - z_{1j}}{1 - \beta_{zj}}\right)\tau} d\tau e^{-i\left(\frac{\omega_1}{1 - \beta_{zj}}\right)k_w a_w} \\ &- \sum_{\nu=\pm 1} \sum_j \frac{\delta(z_1 - z_{1j})}{(1 - \beta_{zj})\gamma_0} \left( \frac{\gamma_b}{2\gamma_0} \right) \sum_{k,a} \frac{g_{ka}}{\sqrt{\omega_k}} \hat{e}^a \int_0^{\tau_1} e^{i\left(\omega_1 - \omega_{ka} + \nu \frac{\omega_s}{1 - \beta_{zj}}\right)\tau} d\tau e^{i\left(\phi_{ka} + \nu \frac{\omega_s}{1 - \beta_{zj}}\right) + \nu \phi_s} f_{ka} \\ &- F \sum_{\nu=\pm 1} \sum_j \frac{\delta(z_1 - z_{1j})}{(1 - \beta_{zj})\gamma_0} \left( \frac{\gamma_b}{2\gamma_0} \right) \int_0^{\tau_1} e^{i\left(\omega_1 - k_w \frac{z_1 - z_{1j}}{1 - \beta_{zj}} + \nu \frac{\omega_s}{1 - \beta_{zj}}\right)\tau} d\tau e^{-i\left(\frac{\omega_1}{1 - \beta_{zj}}\right)(k_w - \nu \frac{\omega_s}{1 - \beta_{zj}}) + \nu \phi_s} a_w \\ &+ H.C.\end{aligned}\quad (11)$$

multiplied by a constant  $K \frac{4\pi}{c} \frac{a_w^2}{m_0 \tau}$ . (The abbreviation H.C. stands for Hermitian conjugate.) In the RHS of the spectral field equation, the taper-dependent term  $e^{-ik_w \frac{z_1 - z_{1j}}{1 - \beta_{zj}}}$  can be extracted from the integral.

After performing the  $r$  integration from 0 to a laser pulse slippage time  $\tau_1$  across the undulator, we obtain the  $i$ th component of the laser equation:

$$\begin{aligned}
& \frac{2g_{k_0}}{\sqrt{\omega_i}} i k \epsilon e^{i\phi_i} \left( \frac{\partial f_i}{\partial z_1} + i \frac{\partial \phi_i}{\partial z_1} f_i \right) \\
&= \frac{4\pi}{c} \frac{e^2}{m_0 c} \frac{g_{k_0}}{\sqrt{\omega_i}} \epsilon \sum_j \frac{\delta(z_1 - z_{1j})}{(1 - \beta_{sj})\gamma_0} e^{i\phi_i} f_i \\
&+ \frac{4\pi}{c} \frac{e^2}{m_0 c} F \sum_j \frac{\delta(z_1 - z_{1j})}{(1 - \beta_{sj})\gamma_0} e^{i\frac{\tau_1}{2} \left( \omega_i - k_w \frac{\beta_{sj} c}{1 - \beta_{sj}} \right)} e^{-i k_w \frac{\delta_j}{1 - \beta_{sj}}} \frac{\sin \frac{\tau_1}{2} \left( \omega_i - k_w \frac{\beta_{sj} c}{1 - \beta_{sj}} \right)}{\frac{\tau_1}{2} \left( \omega_i - k_w \frac{\beta_{sj} c}{1 - \beta_{sj}} \right)} a_w \\
&- \frac{4\pi}{c} \frac{e^2}{m_0 c} \sum_{\nu=\pm 1} \sum_j \frac{g_{k'}}{\sqrt{\omega_i + \nu \frac{\omega_{sj}}{1 - \beta_{sj}}}} i \frac{\delta(z_1 - z_{1j})}{(1 - \beta_{sj})\gamma_0} \left( \frac{\gamma_{sj}}{2\gamma_0} \right) e^{i \left( \phi_{k'} + \nu \frac{\omega_{sj}}{c} \frac{\delta_j}{1 - \beta_{sj}} + \nu \phi_e \right)} f_{k'} \\
&- \frac{4\pi}{c} \frac{e^2}{m_0 c} \sum_{\nu=\pm 1} F \sum_j \frac{\delta(z_1 - z_{1j})}{(1 - \beta_{sj})\gamma_0} \left( \frac{\gamma_{sj}}{2\gamma_0} \right) e^{i\frac{\tau_1}{2} \left( \omega_i - k_w \frac{\beta_{sj} c}{1 - \beta_{sj}} + \nu \frac{\omega_{sj}}{1 - \beta_{sj}} \right)} e^{-i \left( \frac{\delta_j}{1 - \beta_{sj}} \right) \left( k_w - \nu \frac{\omega_{sj}}{c} \right) + \nu \phi_e} \\
&\times \frac{\sin \frac{\tau_1}{2} \left( \omega_i - k_w \frac{\beta_{sj} c}{1 - \beta_{sj}} + \nu \frac{\omega_{sj}}{1 - \beta_{sj}} \right)}{\frac{\tau_1}{2} \left( \omega_i - k_w \frac{\beta_{sj} c}{1 - \beta_{sj}} + \nu \frac{\omega_{sj}}{1 - \beta_{sj}} \right)} a_w, \tag{12}
\end{aligned}$$

where

$$ck' \equiv \omega_i' = \omega_i + \nu \frac{\omega_{sj}}{1 - \beta_{sj}}. \tag{13}$$

The first and second terms on the RHS are present even without synchrotron oscillation. The third and fourth terms, which have a multiplier of synchrotron oscillation, represent the effect resulting from the synchrotron oscillation.

We multiply by  $e^{-i\phi_i}$  and separate real and imaginary parts. The real part gives an equation for phase:

$$\begin{aligned}
& \frac{-2g_{k_0}}{\sqrt{\omega_i}} k \frac{\partial \phi_i}{\partial z_1} f_i \\
&= \frac{4\pi}{c} \frac{e^2}{m_0 c} \frac{g_{k_0}}{\sqrt{\omega_i}} \sum_j \frac{\delta(z_1 - z_{1j})}{(1 - \beta_{sj})\gamma_0} f_i \\
&+ \frac{4\pi}{c} \frac{e^2}{m_0 c} (F \cdot \epsilon) \sum_j \frac{\delta(z_1 - z_{1j})}{(1 - \beta_{sj})\gamma_0} \cos \left[ \frac{\tau_1}{2} \left( \omega_i - k_w \frac{\beta_{sj} c}{1 - \beta_{sj}} \right) - k_w \frac{\delta_j}{1 - \beta_{sj}} - \phi_i \right] \frac{\sin \frac{\tau_1}{2} \left( \omega_i - k_w \frac{\beta_{sj} c}{1 - \beta_{sj}} \right)}{\frac{\tau_1}{2} \left( \omega_i - k_w \frac{\beta_{sj} c}{1 - \beta_{sj}} \right)} a_w \\
&- \frac{4\pi}{c} \frac{e^2}{m_0 c} \sum_{\nu=\pm 1} \sum_j \frac{g_{k'}}{\sqrt{\omega_i + \nu \frac{\omega_{sj}}{1 - \beta_{sj}}}} \frac{\delta(z_1 - z_{1j})}{(1 - \beta_{sj})\gamma_0} \left( \frac{\gamma_{sj}}{2\gamma_0} \right) \cos \left( \phi_{k'} - \phi_i + \nu \frac{\omega_{sj}}{c} \frac{\delta_j}{1 - \beta_{sj}} + \nu \phi_e \right) f_{k'} \\
&- \frac{4\pi}{c} \frac{e^2}{m_0 c} \sum_{\nu=\pm 1} (F \cdot \epsilon) \sum_j \frac{\delta(z_1 - z_{1j})}{(1 - \beta_{sj})\gamma_0} \left( \frac{\gamma_{sj}}{2\gamma_0} \right) \\
&\times \cos \left[ \frac{\tau_1}{2} \left( \omega_i - k_w \frac{\beta_{sj} c}{1 - \beta_{sj}} + \nu \frac{\omega_{sj}}{1 - \beta_{sj}} \right) - \left( \frac{\delta_j}{1 - \beta_{sj}} \right) \left( k_w - \nu \frac{\omega_{sj}}{c} \right) - \phi_i + \nu \phi_e \right] \\
&\times \frac{\sin \frac{\tau_1}{2} \left( \omega_i - k_w \frac{\beta_{sj} c}{1 - \beta_{sj}} + \nu \frac{\omega_{sj}}{1 - \beta_{sj}} \right)}{\frac{\tau_1}{2} \left( \omega_i - k_w \frac{\beta_{sj} c}{1 - \beta_{sj}} + \nu \frac{\omega_{sj}}{1 - \beta_{sj}} \right)} a_w. \tag{14}
\end{aligned}$$

The imaginary part gives an amplitude equation:

$$\begin{aligned}
& \frac{2g_{k_0}}{\sqrt{\omega_i}} k \frac{\partial f_i}{\partial z_1} \\
&= \frac{4\pi}{c} \frac{e^2}{m_0 c} (F \cdot \epsilon) \sum_j \frac{\delta(z_1 - z_{1j})}{(1 - \beta_{sj})\gamma_0} \sin \left[ \frac{\tau_1}{2} \left( \omega_i - k_w \frac{\beta_{sj} c}{1 - \beta_{sj}} \right) - k_w \frac{\delta_j}{1 - \beta_{sj}} - \phi_i \right] \frac{\sin \frac{\tau_1}{2} \left( \omega_i - k_w \frac{\beta_{sj} c}{1 - \beta_{sj}} \right)}{\frac{\tau_1}{2} \left( \omega_i - k_w \frac{\beta_{sj} c}{1 - \beta_{sj}} \right)} a_w \\
&- \frac{4\pi}{c} \frac{e^2}{m_0 c} \sum_{\nu=\pm 1} \sum_j \frac{g_{k'}}{\sqrt{\omega_i + \nu \frac{\omega_{sj}}{1 - \beta_{sj}}}} \frac{\delta(z_1 - z_{1j})}{(1 - \beta_{sj})\gamma_0} \left( \frac{\gamma_{sj}}{2\gamma_0} \right) \sin \left( \phi_{k'} - \phi_i + \nu \frac{\omega_{sj}}{c} \frac{\delta_j}{1 - \beta_{sj}} + \nu \phi_e \right) f_{k'}
\end{aligned}$$

$$\begin{aligned}
& -\frac{4\pi}{c} \frac{e^2}{m_0 c} \sum_{\nu=\pm 1} (\mathbf{F} \cdot \hat{\epsilon}) \sum_j \frac{\delta(z_1 - z_{1j})}{(1 - \beta_{zj})\gamma_0} \left( \frac{\gamma_{bj}}{2\gamma_0} \right) \\
& \times \sin \left[ \frac{\tau_1}{2} \left( \omega_i - k_w \frac{\beta_{zj} c}{1 - \beta_{zj}} + \nu \frac{\omega_{sj}}{1 - \beta_{zj}} \right) - \left( \frac{\delta_j}{1 - \beta_{zj}} \right) (k_w - \nu \frac{\omega_{sj}}{c}) - \phi_i + \nu \phi_e \right] \\
& \times \frac{\sin \frac{\tau_1}{2} \left( \omega_i - k_w \frac{\beta_{zj} c}{1 - \beta_{zj}} + \nu \frac{\omega_{sj}}{1 - \beta_{zj}} \right)}{\tau_1 \left( \omega_i - k_w \frac{\beta_{zj} c}{1 - \beta_{zj}} + \nu \frac{\omega_{sj}}{1 - \beta_{zj}} \right)} a_w .
\end{aligned} \tag{15}$$

In both the amplitude and the phase equations, there are two types of frequency-dependent terms. They are

$$\frac{\sin \delta_{i\nu}}{\delta_{i\nu}}, \quad \sin(X_{i\nu} + \phi_i), \quad \text{and} \quad \cos(X_{i\nu} + \phi_i),$$

where  $X_{i\nu}$  and  $\delta_{i\nu}$  are given by

$$X_{i\nu} = -\frac{\tau_1}{2} [\omega_i - (\omega_p - \nu \omega_s')] + k_w \frac{\delta}{1 - \beta_z}$$

and

$$\begin{aligned}
\delta_{i\nu} &= +\frac{\tau_1}{2} [\omega_i - (\omega_p - \nu \omega_s')] , \\
&\text{where } \nu = 0, +1, \text{ and } -1 .
\end{aligned} \tag{16}$$

The  $\omega_p$  and  $\omega_s'$  are given as

$$\omega_p = \frac{k_w \beta_z c}{1 - \beta_z} \text{ and } \omega_s' = \frac{\omega_s}{1 - \beta_z} . \tag{17}$$

Using  $X_{i\nu}$  and  $\delta_{i\nu}$ , Eqs. (14) and (15) simplify to

$$\begin{aligned}
& \frac{-2g_1}{\sqrt{\omega_i}} k \frac{\partial \phi_1}{\partial z_1} f_1 \\
& = \frac{4\pi}{c} \frac{e^2}{m_0 c} \frac{g_1}{\sqrt{\omega_i}} \sum_j \frac{\delta(z_1 - z_{1j})}{(1 - \beta_{zj})\gamma_0} f_1 \\
& + \frac{4\pi}{c} \frac{e^2}{m_0 c} (\mathbf{F} \cdot \hat{\epsilon}) \sum_j \frac{\delta(z_1 - z_{1j})}{(1 - \beta_{zj})\gamma_0} \cos(X_{i0} + \phi_i) \frac{\sin \delta_{i0}}{\delta_{i0}} a_w \\
& - \frac{4\pi}{c} \frac{e^2}{m_0 c} \sum_{\nu=\pm 1} \sum_j \frac{g_{k'}}{\sqrt{\omega_i + \nu \frac{\omega_{sj}}{1 - \beta_{zj}}}} \frac{\delta(z_1 - z_{1j})}{(1 - \beta_{zj})\gamma_0} \left( \frac{\gamma_{bj}}{2\gamma_0} \right) \cos \left( \phi_{k'} - \phi_i + \nu \frac{\omega_{sj}}{c} \frac{\delta_j}{1 - \beta_{zj}} + \nu \phi_e \right) f_{k'} \\
& - \frac{4\pi}{c} \frac{e^2}{m_0 c} \sum_{\nu=\pm 1} (\mathbf{F} \cdot \hat{\epsilon}) \sum_j \frac{\delta(z_1 - z_{1j})}{(1 - \beta_{zj})\gamma_0} \left( \frac{\gamma_{bj}}{2\gamma_0} \right) \cos \left( X_{i\nu} + \phi_i - \nu \frac{\omega_{sj}}{c} \frac{\delta_j}{1 - \beta_{zj}} - \nu \phi_e \right) \frac{\sin \delta_{i\nu}}{\delta_{i\nu}} a_w .
\end{aligned} \tag{18}$$

and

$$\begin{aligned}
& \frac{2g_1}{\sqrt{\omega_i}} k \frac{\partial f_1}{\partial z_1} \\
& = -\frac{4\pi}{c} \frac{e^2}{m_0 c} (\mathbf{F} \cdot \hat{\epsilon}) \sum_j \frac{\delta(z_1 - z_{1j})}{(1 - \beta_{zj})\gamma_0} \sin(X_{i0} + \phi_i) \frac{\sin \delta_{i0}}{\delta_{i0}} a_w \\
& - \frac{4\pi}{c} \frac{e^2}{m_0 c} \sum_{\nu=\pm 1} \sum_j \frac{g_{k'}}{\sqrt{\omega_i + \nu \frac{\omega_{sj}}{1 - \beta_{zj}}}} \frac{\delta(z_1 - z_{1j})}{(1 - \beta_{zj})\gamma_0} \left( \frac{\gamma_{bj}}{2\gamma_0} \right) \sin \left( \phi_{k'} - \phi_i + \nu \frac{\omega_{sj}}{c} \frac{\delta_j}{1 - \beta_{zj}} + \nu \phi_e \right) f_{k'} \\
& + \frac{4\pi}{c} \frac{e^2}{m_0 c} \sum_{\nu=\pm 1} (\mathbf{F} \cdot \hat{\epsilon}) \sum_j \frac{\delta(z_1 - z_{1j})}{(1 - \beta_{zj})\gamma_0} \left( \frac{\gamma_{bj}}{2\gamma_0} \right) \sin \left( X_{i\nu} + \phi_i - \nu \frac{\omega_{sj}}{c} \frac{\delta_j}{1 - \beta_{zj}} - \nu \phi_e \right) \frac{\sin \delta_{i\nu}}{\delta_{i\nu}} a_w .
\end{aligned} \tag{19}$$

The second expression of Eq. (17) relates the periodic oscillation frequency  $\omega_s$ , such as the synchrotron frequency, to the corresponding laser frequency shift  $\omega_s'$ . We note that when the laser frequency  $\omega_i$  is equal to the  $\omega_p$ , then  $\frac{\sin \delta_{i\nu}}{\delta_{i\nu}}$  takes its maximum value in the absence of the sideband and, thus, corresponds to the "resonance condition." To show this, we solve  $\omega_i = \omega_p$  by utilizing the relation  $\frac{1}{1 - \beta_z} = \frac{(1 + \beta_z)\gamma^2}{1 + \alpha^2}$ . We obtain

$$k_L = k_w \frac{\beta_z}{1 - \beta_z} = k_w \frac{\beta_z(1 + \beta_z)\gamma^2}{1 + \alpha^2} = k_w \frac{2\gamma^2}{1 + \alpha^2} . \tag{20}$$

When a dominant bucket is formed at high laser intensity, we may assume that the laser phase angle changes slowly. One of the effects of the sideband is that it artificially shifts the bucket with respect to phase, according to the amount of the sideband frequency shift. The spectral function in the driving term is modified by the sideband with  $\nu\omega'_s$ :

$$\frac{\sin \frac{\tau_1}{2} [\omega_i - (\omega_p - \nu\omega'_s)]}{\frac{\tau_1}{2} [\omega_i - (\omega_p - \nu\omega'_s)]} \quad (21)$$

The shift of the spectral function caused by the sideband is

$$\frac{\tau_1}{2} \omega'_s = \frac{1}{2} \frac{L_w}{c\beta_z} (1 - \beta_z) \frac{\omega_s}{1 - \beta_z} = \pi \frac{L_w}{\beta_z L_{sync}} \approx \frac{L_w}{L_{sync}} \pi \quad (22)$$

This equation states that when the frequency chirp caused by the sideband is more than half the laser bandwidth (synchrotron period  $\leq$  undulator length), the driving term passes a node and starts driving the next bandwidth. The strength of the spectral function becomes maximum at every  $\pi$ . When the sidebands are driven by this chirping mechanism, a new sideband appears as the chirping given by Eq. (22) passes each node.

The wavelength chirping of each sideband with respect to the fundamental can be obtained as follows: Using  $\lambda_L = \frac{(1-\beta_z)}{\beta_z} \lambda_w$ , the second part of Eq. (17) becomes

$$\omega'_s = \Delta\omega_L \sim \frac{\lambda_w}{\lambda_L} \omega_s = \frac{\lambda_w}{\lambda_L} \frac{2\pi c}{L_{sync}} \quad (23)$$

Taking the ratio to  $\omega_L$ , converting to wavelength using Eq. (22), and noting that the driving term has nodes at every  $\pi$  in  $\Delta\omega_L$ , we obtain the sideband separations as

$$\frac{\Delta\lambda_L}{\lambda_L} = + \frac{\lambda_w}{L_{sync}} m \quad \text{where } m : \text{integer} > 1 \quad (24)$$

We have included the factor  $m$  to represent the  $m$ th sideband. For example, in the Los Alamos experiment with  $\lambda_w = 2.7$  cm and  $L_{sync} = 1$  m, the quantity  $\frac{\Delta\lambda_L}{\lambda_L}$  is calculated to be  $0.3 \mu\text{m}$ , which is in good agreement with the numerical simulation.

In addition to the sidebands that chirp from the resonant frequency as described above, there appears another class of sidebands. In the following sections, we study the individual driving terms closely and identify the different classes of sidebands.

### Driving Terms Neglecting the Effect from the Electron Bunching

Neglecting the common multiplicative factors, the driving terms of Eq. (19) from the  $j$ th particle by the undulator field can be written as

$$F = \sin(X_{10} + \phi_1) \frac{\sin \delta_{10}}{\delta_{10}} - \left( \frac{\gamma_b}{2\gamma_0} \right) \sin(X_{1\nu} + \phi_1 - \eta - \nu\phi_e) \frac{\sin \delta_{1\nu}}{\delta_{1\nu}} \quad (25)$$

We note that  $k_w \frac{\delta_j}{1-\beta_{zj}} + \phi_1$  is equal to  $(k_L + k_w)z - \omega_L t + \phi_1$ . A negative sign in  $F \cdot \hat{e}$  is included in Eq. (25). The factor  $\eta \equiv \nu \frac{\omega_w}{c} \frac{\delta_j}{1-\beta_{zj}}$  and its ratio to electron phase are relatively small for a 3-cm period and 1-m undulator:

$$\frac{\eta}{k_w \frac{\delta_j}{1-\beta_{zj}}} = \frac{\nu \frac{\omega_w}{c}}{k_w} = \nu \frac{\lambda_w}{L_{sync}} \sim \pm 3\%.$$

Separating the terms within  $\sin$  into one term that includes the frequency and another term that includes the phase angle  $k_w \frac{\delta_j}{1-\beta_{zj}} + \phi_1$ , Eq. (25) is written as

$$\begin{aligned} F = & \sin \left( k_w \frac{\delta_j}{1-\beta_{zj}} + \phi_1 \right) \frac{\cos \frac{\tau_1}{2} (\omega - \omega_p) \sin \frac{\tau_1}{2} (\omega - \omega_p)}{\frac{\tau_1}{2} (\omega - \omega_p)} - \cos \left( k_w \frac{\delta_j}{1-\beta_{zj}} + \phi_1 \right) \frac{\sin^2 \frac{\tau_1}{2} (\omega - \omega_p)}{\frac{\tau_1}{2} (\omega - \omega_p)} \\ & - \left( \frac{\gamma_b}{2\gamma_0} \right) \sin \left( k_w \frac{\delta_j}{1-\beta_{zj}} + \phi_1 - \eta \right) \frac{\cos \left\{ \frac{\tau_1}{2} [\omega - (\omega_p - \nu\omega'_s)] + \nu\phi_e \right\} \sin \frac{\tau_1}{2} [\omega - (\omega_p - \nu\omega'_s)]}{\frac{\tau_1}{2} [\omega - (\omega_p - \nu\omega'_s)]} \\ & + \left( \frac{\gamma_b}{2\gamma_0} \right) \cos \left( k_w \frac{\delta_j}{1-\beta_{zj}} + \phi_1 - \eta \right) \frac{\sin \left\{ \frac{\tau_1}{2} [\omega - (\omega_p - \nu\omega'_s)] + \nu\phi_e \right\} \sin \frac{\tau_1}{2} [\omega - (\omega_p - \nu\omega'_s)]}{\frac{\tau_1}{2} [\omega - (\omega_p - \nu\omega'_s)]} \end{aligned} \quad (26)$$

For an ideal untapered undulator, the resonant angle is zero. We make the assumption that the resonant angle  $k_w \frac{\delta_j}{1-\beta_{zj}} + \phi_1$  is equal to zero for all buckets, including those arising from the sidebands. This assumption is reasonable because the undulator taper determines the resonant angle. With this assumption, a sum over particles is zero:

$$\int \sum_j \sin \left( k_w \frac{\delta_j}{1-\beta_{zj}} + \phi \right) dz' = 0.$$



The driving expression is further simplified to

$$F \simeq -\cos\left(k_u \frac{\delta_j}{1-\beta_{zj}} + \phi_i\right) \frac{\sin^2 \frac{\pi}{2}(\omega - \omega_p)}{\frac{\pi}{2}(\omega - \omega_p)} + \left(\frac{\gamma b}{2\gamma_0}\right) \cos\left(k_u \frac{\delta_j}{1-\beta_{zj}} + \phi_i - \eta\right) \times \frac{\sin\left\{\frac{\pi}{2}[\omega - (\omega_p - \nu\omega'_s)] + \nu\phi_e\right\} \sin \frac{\pi}{2}[\omega - (\omega_p - \nu\omega'_s)]}{\frac{\pi}{2}[\omega - (\omega_p - \nu\omega'_s)]} \quad (27)$$

Two driving terms are characterized by the presence or absence of  $\nu\omega'_s$ . The first term in Eq. (27) has no dependence on  $\omega'_s$ . For the second term, the spectrum is displaced by  $\omega'_s$ , but it maintains its spectral shape. Also, the amplitude of this term depends on the amplitude of the average energy oscillation, which is expected to be, at most, a relative half-energy spread of the dominant bucket.

Although the initial phase  $\phi_e$  is determined by when the electrons effectively start bunching along the undulator, we can understand the sideband chirping better by approximating  $\phi_e = \pi$ . By doing so, the phase of excited waves from the first "stationary term" and from the second "chirping term" are equal at the limit  $\omega'_s = 0$ . Both terms have the same spectral shape with its origin coinciding at the limit  $\omega'_s = 0$ . The spectral shape of the stationary and chirping terms are shown in Fig. 1. They are centered at wavelength 10.14  $\mu\text{m}$ , and the chirping term shown as a dashed line is also centered at 10.14  $\mu\text{m}$ . At this limit  $\omega'_s = 0$ , nodes and peaks for both spectra coincide.

The chirping term with  $\nu = 1$  chirps to a longer wavelength from the center, and it enhances the amplitudes created by the stationary term as its peak sweeps over the local peaks of the stationary spectrum. The chirping term with  $\nu = -1$  chirps to a shorter wavelength from the center, and it cancels the amplitudes created by the stationary term because the phase of the stationary term is opposite to the phase of the chirping term. The phase of waves at a wavelength less than the center is driven by the stationary term  $\pi$  away from the phase of waves at a wavelength longer than the center.

The stationary term drives more strongly at local peaks that locate symmetrically from the resonant wavelength than at the chirping term. Each local peak of the stationary spectrum drives the sideband; this class of sidebands develops independently from the synchrotron oscillation. As the total laser power increases, a number of sidebands appear, even when the ratio of undulator length to synchrotron length is about one or two.

The chirping spectrum enhances the waves excited by the stationary spectrum and also creates its own local peaks. The frequency of sidebands driven by the chirping terms degenerates from the main peaks of the stationary term. The amount of chirp is determined by Eq. (22). The peak of the laser amplitude spectrum chirps to a longer wavelength according to the peak of the chirping spectrum.

Figure 2 shows the driver  $F$  as a function of synchrotron length  $L_{sync}$ . As the chirping term chirps in the wavelength according to the synchrotron length, its peak traces the spectrum of the stationary term. The effect of the sideband gradually increases and peaks at  $2L_{wig} = L_{sync}$ ; when the intensity becomes larger, the stationary driving term reduces and becomes zero at  $L_{wig} = L_{sync}$ . Successive peaks are at  $L_{wig} = L_{sync}(n + \frac{1}{2})$ . The displacement of wavelength caused by chirping for a sideband from  $\lambda_p$ , defined as  $\frac{2\pi c}{\omega_p}$ , is obtained by using Eq. (23):

$$\frac{\delta\lambda_{side}}{\lambda_p} = \frac{\lambda_u}{L_{sync}} = \frac{x}{N} \quad (28)$$

where  $x \equiv L_u/L_{sync}$  and  $N$  is the number of periods in an undulator. The fractional wavelength separation between successive peaks is  $\lambda_u/L_{sync}$ .

Because the spectrum has a shape  $\frac{\sin^2 x}{x}$ , the wavelength of successive local peaks of the driver can be obtained by solving

$$x - \tan x = 0.$$

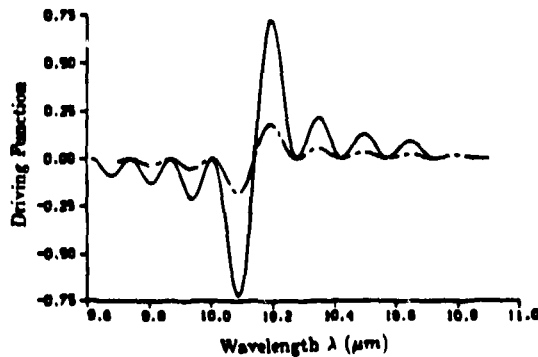


Fig. 1. The spectral shapes of the stationary term and the chirping term are the same, and the center coincides at  $\omega'_s = 0$ .

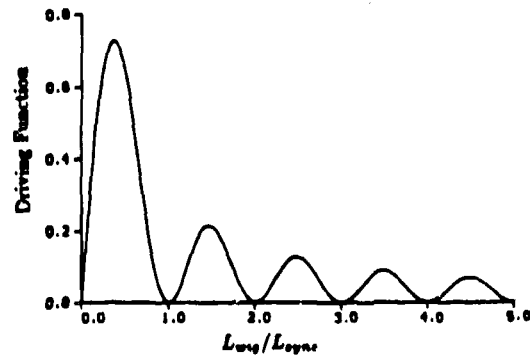


Fig. 2. The stationary driving term is periodic as a function of  $\frac{L_{wig}}{L_{sync}}$ .

The relation between  $x$  and laser wavelength  $\lambda_L$  is given by

$$\lambda_L = \frac{\lambda_{L0}}{1 + x \frac{\lambda_u}{\pi L_{sync}}} \quad (29)$$

where the  $\lambda_{L0}$  is the resonant wavelength.

### Comparison of Local Spectral Peaks between Numerical Simulation and the Theory for an Untapered Undulator

In the previous section, we have derived several characteristics of the sideband for an untapered undulator. We now compare the local peaks of the spectra obtained from the numerical simulation using FELP and the local peaks calculated from the analytical expression.

#### Initial Conditions for Running FEL Multipass Simulation with the Code FELP

We simulate the multipass process using the code FELP with the following assumptions: (1) cavity loss is set to zero, (2) the electric field is driven with random noise at the first pass, and (3) the assumed undulator is of the Halbach type.<sup>2</sup> We ran the code FELP under the periodic mode where the boundary conditions for both the electron beam and the laser are assumed periodic. Initial conditions are shown in the following list:

Electron-beam peak current	150 A
Electron-beam energy ( $\gamma = \frac{E}{mc^2}$ )	41.8
Undulator field	3 kG
Undulator length	200 cm
Undulator wavelength	2.73 cm
Rayleigh range	49.5 cm

The resonant wavelength  $\lambda_L$  of the system including the Gaussian-wave effect is calculated to be 10.14  $\mu\text{m}$ .

#### Wavelength Shift of the Spectrum for the Chirping Term

The second part of Eq. (17), which gives the laser frequency shift of the driving spectra, can be rewritten in terms with wavelength using Eq. (20) as

$$\omega'_s = \frac{\lambda_u}{\lambda_L} \frac{2\pi c}{L_{sync}} \quad (30)$$

where  $\lambda_L$  and  $\lambda_u$  are laser and undulator wavelengths. The laser wavelength after the shift is then expressed as

$$\begin{aligned} \lambda_{newL} &= \lambda_L \frac{1}{\left(1 - \nu \frac{\lambda_u}{L_{sync}}\right)} \\ &= \lambda_L \frac{1}{\left(1 - \nu \frac{1}{N} \frac{L_{sync}}{L_{sync}}\right)} \end{aligned} \quad (31)$$

where  $N$  is the number of periods in the undulator ( $= \frac{L_{sync}}{\lambda_u}$ ) and the index  $\nu$  can be either +1 or -1. With respect to resonant laser wavelength  $\lambda_L = 10.14 \mu\text{m}$ , the wavelength shift  $\delta\lambda_L$  is approximately linear in  $\frac{L_{sync}}{L_{sync}}$ , as shown in Fig. 3. For example, the wavelength shifts by 0.3  $\mu\text{m}$  at  $L_{sync} = L_{wig}$ .

As the power present in the FEL cavity increases, the synchrotron length decreases. Assuming a no-loss cavity, Fig. 4 shows the number of synchrotron periods in an undulator length plotted as a function of power. At 1 GW power, about two synchrotron oscillations take place in the undulator. For this no-loss system, it takes about 100 passes to reach 5 GW with the FELP code. The pass number is plotted against the power in Fig. 5. The intensity was assumed to be  $10^4 \text{ W/cm}^2$  at the entrance to the undulator.

#### The Sidebands by the Stationary Term and by the Chirping Term

In the following argument, we ignore the dependence on the electron distribution and the laser phase because they are not obtainable analytically in terms of simple expressions. However, they affect the relative strength of the driving terms; that is, they enhance the chirping sideband drivers.

In the numerical simulation, we take snapshots of the laser electric field spectrum at Pass 1, Pass 7, Pass 20, Pass 100, and Pass 200. The growth of the sidebands is associated with the synchrotron length and the wavelength chirp. The laser spectrum at Pass 1 is shown in Fig. 6. The optical power is  $1.572 \times 10^4 \text{ W}$ , and gain is about 100. The synchrotron length is approximately 1997 cm, and  $\frac{L_{sync}}{L_{sync}}$  is 0.1. The wavelength shift is 0.014  $\mu\text{m}$ . The peak of electric field amplitude is at 10.18  $\mu\text{m}$ , the sideband with a  $\pi$  phase shift is seen at 10.10  $\mu\text{m}$ . Although it is not clear, we also see that the

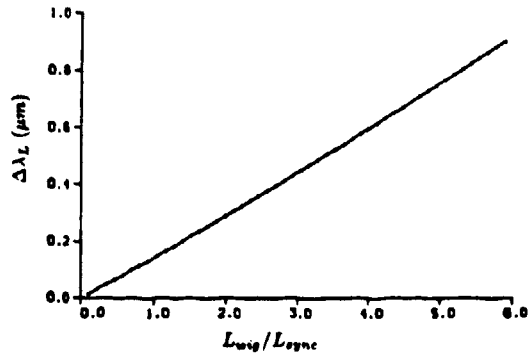


Fig. 3. The wavelength chirp of the chirping term is proportional to the factor  $\frac{L_{wig}}{L_{sync}}$ .

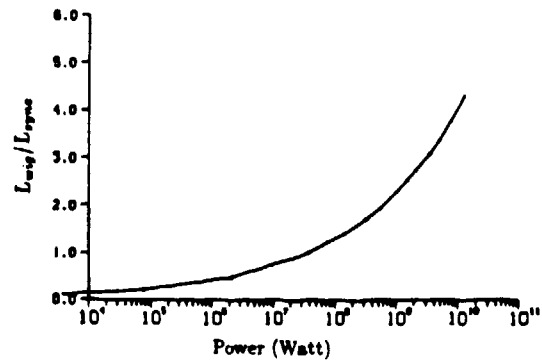


Fig. 4. The inverse of the synchrotron period is shown as a function of laser power in a no-loss cavity.

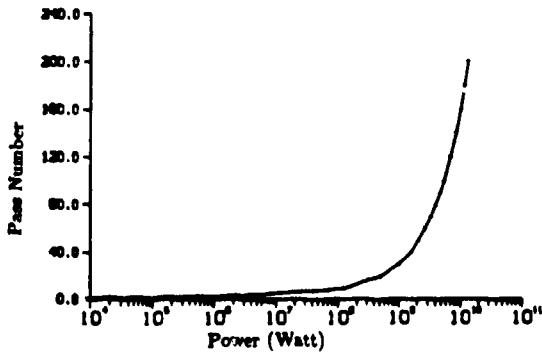


Fig. 5. The pass number is shown as a function of laser power in a no-loss cavity.

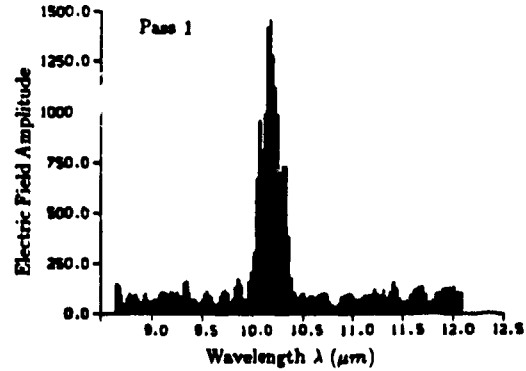


Fig. 6. The laser spectrum at Pass 1.

sideband near  $10.33 \mu\text{m}$  is rising. At this laser power, three driving spectra are well overlapped, as was shown in Fig. 1. The electron energy spectrum is symmetric with respect to the average, as shown in Fig. 7.

The laser spectrum at Pass 7 is shown in Fig. 8. The optical power is  $6.57 \times 10^7 \text{ W}$ , and the gain per pass is about 30%. The ratio  $\frac{L_{wig}}{L_{sync}}$  is 0.997. It has a peak at  $10.2 \mu\text{m}$ . We observe local peaks at  $10.34 \mu\text{m}$  and at  $10.48 \mu\text{m}$ . Also there is a weak local peak at  $10.05 \mu\text{m}$ . To interpret these local peaks from FELP simulation, we calculated the local peaks of the stationary term and the chirping terms. Figure 9 compares the positions of the local peaks: from the stationary spectrum (Case 1), from the spectrum chirping to longer wavelength (Case 2), from the spectrum chirping to shorter wavelength (Case 3), and from the FELP calculation (Case 4). The resonant wavelength is labeled by  $C_0$ , the centers of chirping spectra are labeled by  $C$ . The numerical resolution is shown as horizontal arrows at points for Case 4. All the local peaks of FELP lie on one or another of the predictions from the driving terms, showing that the weak local peak at  $10.05 \mu\text{m}$  is driven by the term that chirps to shorter wavelength. Other local peaks from FELP coincide with the local peaks of the driving terms. Because they are approximately at the same wavelengths, we cannot identify which term is driving the peaks. We note that several sidebands are already observed at synchrotron length approximately equal to the undulator length. The electron energy distribution is shown in Fig. 10. Because of gain, the energy distribution is asymmetric and weighted toward lower energy.

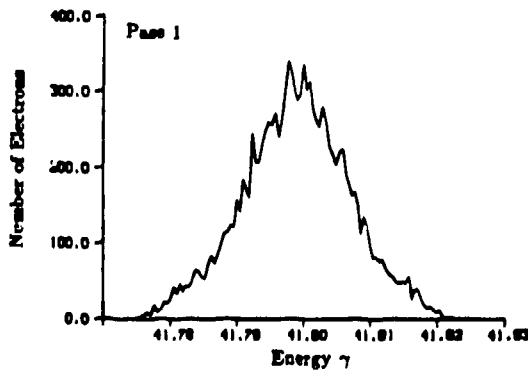


Fig. 7. The electron energy distribution at Pass 1 is nearly symmetric.

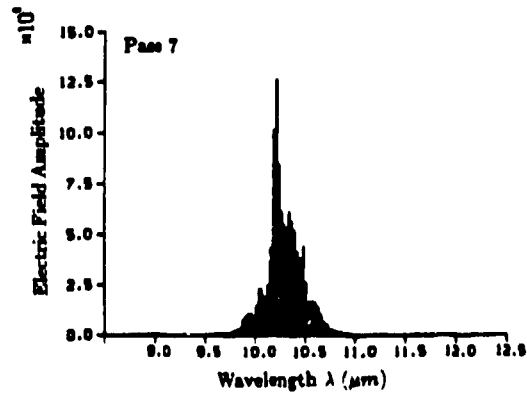


Fig. 8. The laser spectrum at Pass 7 shows that sidebands start appearing.

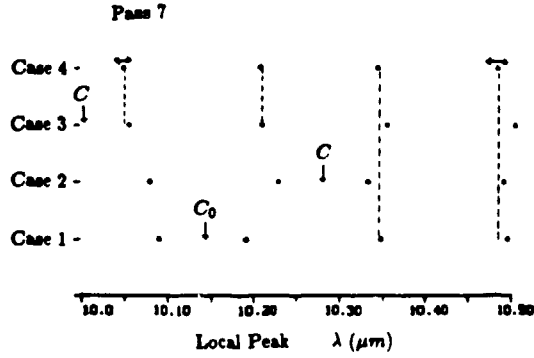


Fig. 9. The local peaks of the stationary driver and the chirping drivers are compared with a numerical simulation (FELP) at Pass 7.

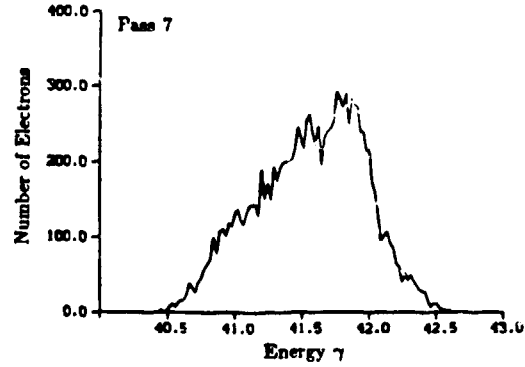


Fig. 10. The electron energy distribution at Pass 7 shows an energy loss.

The chirping term at Pass 20 chirped  $\Delta\lambda = 0.239 \mu\text{m}$  and  $\Delta\lambda = -0.228 \mu\text{m}$ . The stationary term and the term chirped to longer wavelength are shown in Fig. 11; the stationary term and the term chirped to shorter wavelength are shown in Fig. 12. The laser amplitude spectrum has a number of local peaks, as shown in Fig. 13. The optical power is  $5.4 \times 10^8 \text{ W}$ , and the gain per pass is about 9.0%. The ratio  $\frac{L_{\text{wta}}}{L_{\text{pnc}}}$  is 1.69 and has a peak at  $10.48 \mu\text{m}$ . We observe a number of local peaks. All the local peaks from FELP are shown in Fig. 14 as Case 4 together with the local peaks from the stationary term and the chirping terms. Figure 14 shows that the stationary term explains all of the peaks, but the term chirping to a longer wavelength predicts well near  $10.2 \mu\text{m}$ . We note that the chirped center of the term to longer wavelength is about  $10.4 \mu\text{m}$ , and this is approximately close to the weighted center of the FELP spectrum. The electron energy distribution is shown in Fig. 15: the spectrum has developed a wide bandwidth.

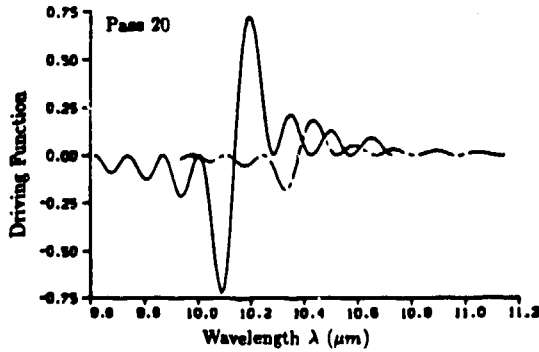


Fig. 11. The term chirped to a longer wavelength is shown with respect to the stationary term at Pass 20.

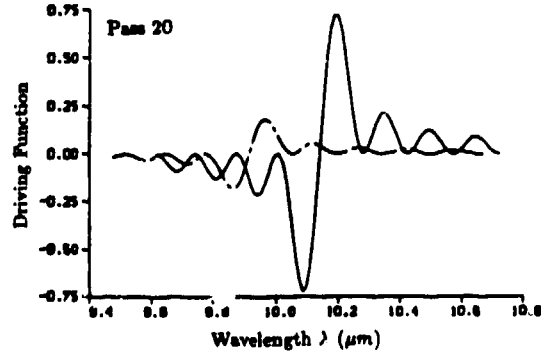


Fig. 12. The term chirped to a shorter wavelength is shown with respect to the stationary term at Pass 20.

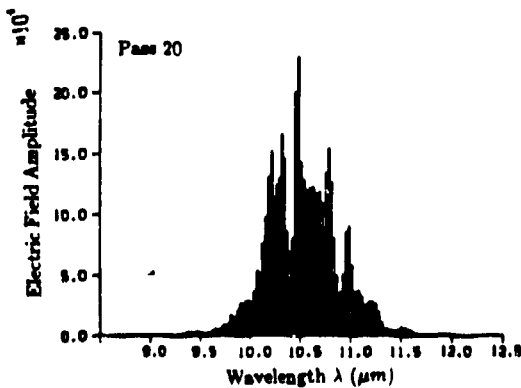


Fig. 13. The laser spectrum at Pass 20 shows a number of sidebands.

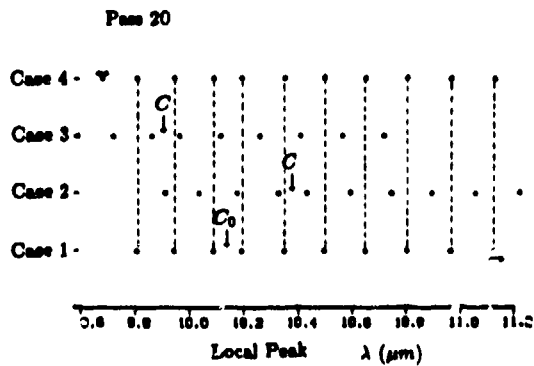


Fig. 14. At Pass 20, the local sideband peaks from FELP simulation can be explained by the stationary term.

The chirping term at Pass 100 chirped  $\Delta\lambda = 0.436 \mu\text{m}$ , and  $\Delta\lambda = -0.402 \mu\text{m}$ . The stationary term and the term chirped to a longer wavelength are shown in Fig. 16; the stationary term and the term chirped to a shorter wavelength are shown in Fig. 17. The laser amplitude spectrum developed more local peaks, as shown in Fig. 18. The optical power is  $5.54 \times 10^9 \text{ W}$ , and the gain per pass is about 1.17%. The ratio  $\frac{L_{\text{max}}}{L_{\text{min}}}$  is 3.02. Figure 18 has two dominant peaks: at  $10.48 \mu\text{m}$  and at  $10.93 \mu\text{m}$ . Figure 19 shows all the local peaks from FELP and the predicted positions of local peaks. At the short wavelength near  $9.6 \mu\text{m}$ , the waves with phase shifted by  $\pi$  are driven either by the stationary term or by the term chirped to a shorter wavelength. At the local peaks with a long wavelength near  $11.5 \mu\text{m}$ , the local peaks by FELP can be explained with the term chirped to a longer wavelength. We also notice that the center of the term chirped to a longer wavelength is at  $10.58 \mu\text{m}$ , which is approximately at the weighted center of the electric-field spectrum. The electron energy spectrum at this pass is shown in Fig. 20. The spectrum has a wide plateau in the center.

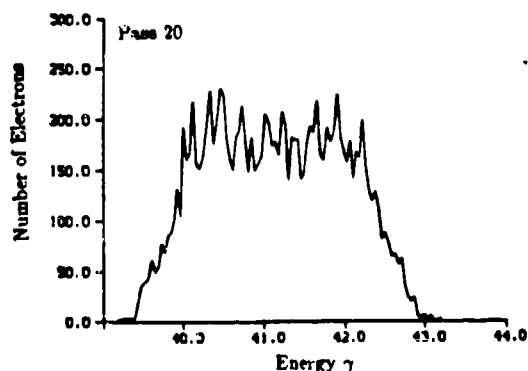


Fig. 15. The energy width of the electron energy distribution increased at Pass 20.

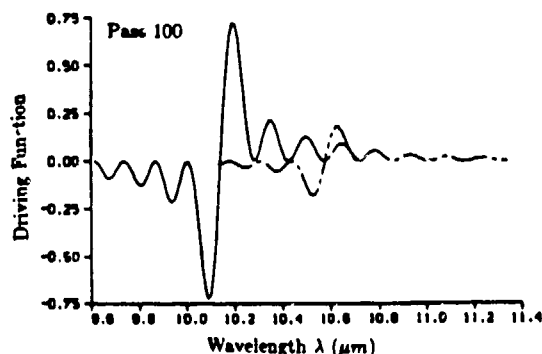


Fig. 16. The term chirped to a longer wavelength is shown with respect to the stationary term at Pass 100.

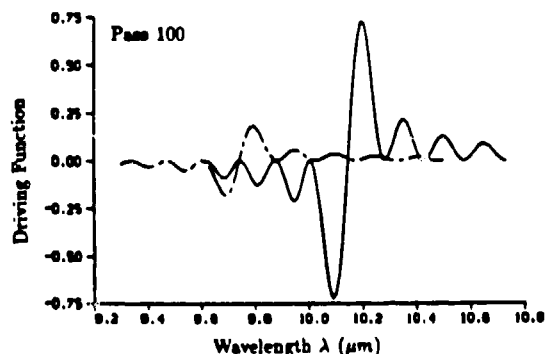


Fig. 17. The term chirped to a shorter wavelength is shown with respect to the stationary term at Pass 100.

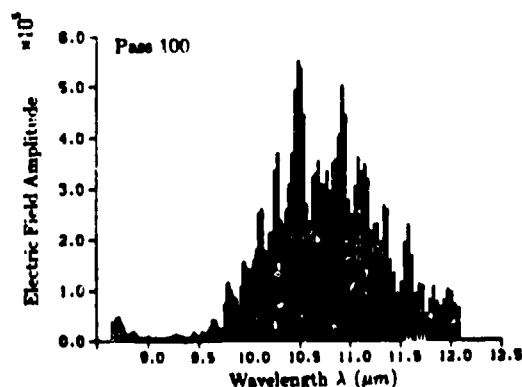


Fig. 18. The laser spectrum shows a number of sidebands at Pass 100.

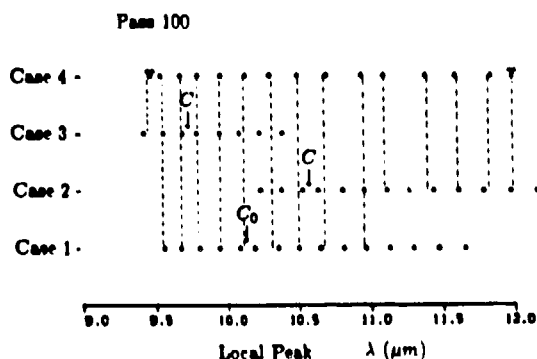


Fig. 19. The local peaks of laser spectrum from numerical simulation (FELP) are predicted from the local peaks of three driving terms at Pass 100.

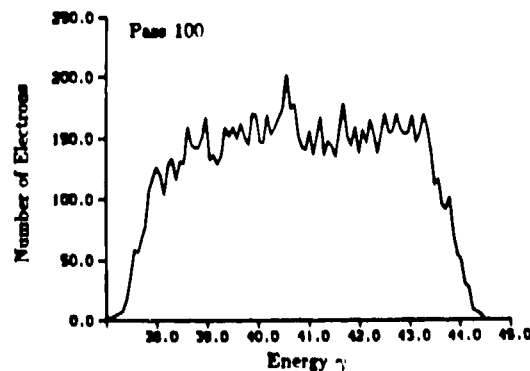


Fig. 20. The electron energy distribution at Pass 100.

At Pass 200, the chirping term chirped by  $\Delta\lambda = 0.540 \mu\text{m}$  and  $\Delta\lambda = -0.488 \mu\text{m}$ . The stationary term and the term chirped to a longer wavelength are shown in Fig. 21; the stationary term and the term chirped to a shorter wavelength are shown in Fig. 22. The spectrum of laser amplitude is richer in structure, as shown in Fig. 23. The optical power is  $1.24 \times 10^{10} \text{ W}$ , and the gain per pass is about 0.57%. The ratio  $\frac{L_{\text{und}}}{L_{\text{syn}}}$  is 3.70. The major peaks are near  $10.68 \mu\text{m}$ , which is the center of the chirping term to a longer wavelength. Figure 24 shows all the local peaks from FELP and the predicted positions of the local peaks. At the short wavelength near  $9.6 \mu\text{m}$ , either the stationary term or the chirped term to a longer wavelength explains the FELP data. Near the major peaks, the stationary term predicts the local peaks. At the longer wavelength limit near  $11.5 \mu\text{m}$ , the term chirped to a longer wavelength appears matched to the FELP data. The electron energy spectrum at this pass (shown in Fig. 25) has a wide plateau in the center and a peak at the low-energy end.

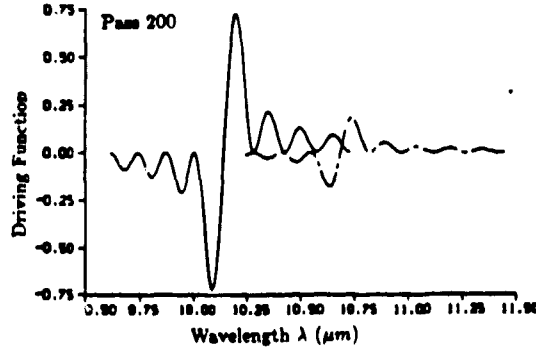


Fig. 21. The term chirped to a longer wavelength is shown with respect to the stationary term at Pass 200.

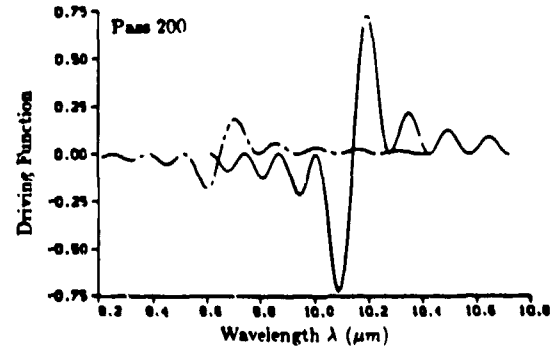


Fig. 22. The term chirped to a shorter wavelength is shown with respect to the stationary term at Pass 200.

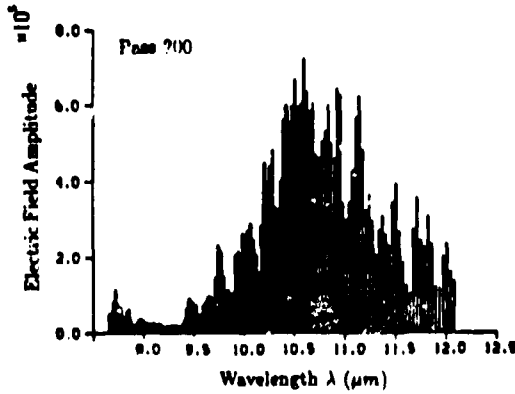


Fig. 23. The laser spectrum at Pass 200.

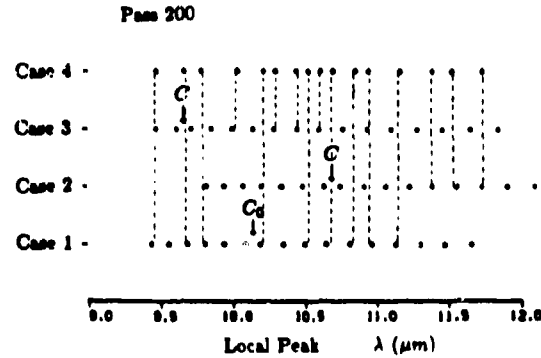


Fig. 24. At Pass 200, the term chirped to a longer wavelength explains the long wavelength end of the FELP local peaks. At the short wavelength end, either the stationary or the term chirped to a shorter wavelength explains the numerical simulation.

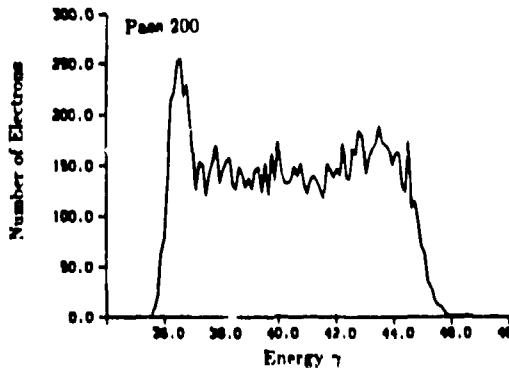


Fig. 25. At Pass 200, the peak near  $\gamma = 37$  in the electron energy distribution shows an electron trapping by the sidebands.

## Conclusion

The analytical theory predicts that the driving terms of sidebands generated in the untapered undulator are classified into two categories: (1) the stationary term that is present even in the absence of synchrotron oscillations and (2) the chirping terms that are driven by the synchrotron oscillations. The relative wavelength separation of the sidebands is determined by the ratio of the undulator wavelength to the synchrotron length for both types of sidebands. The frequencies of the chirping terms degenerates from the stationary term in opposite directions from the resonant frequency as the intensity of the laser increases. The sideband spectrum at a particular laser intensity is a result of a superposition of stationary and chirping sideband drivers.

The numerical simulation of sidebands agreed well with the analytical prediction of the local peaks of the spectrum. In the numerical simulation, laser spectra are calculated by taking snapshots at pass numbers up to 200. For each snapshot, we calculated the synchrotron length and the frequency shift of the driving terms. We calculated all the local peaks as predicted by the three driving terms at each intensity. We then compared those peaks with the local peaks obtained from the numerical simulation. For all the passes where snapshots were taken, they agreed well.

#### **References**

1. H. Takeda, Proc. 1985 FEL Conf., Nucl. Instrum. & Methods **A250**, 476-483 (1986).
2. K. Halbach, Nucl. Instrum. & Methods **187**, 109 (1981).